

Front instabilities in evaporatively dewetting nanofluids

I. Vancea^{*} and U. Thiele[†]

Department of Mathematical Sciences, Loughborough University, Leicestershire LE11 3TU, United Kingdom and Max-Planck-Institut für Physik komplexer Systeme, Nöthnitzer Strasse 38, D-01187 Dresden, Germany

E. Pauliac-Vaujour, A. Stannard, C. P. Martin, M. O. Blunt, and P. J. Moriarty

The School of Physics and Astronomy, The University of Nottingham, Nottingham NG7 2RD, United Kingdom

(Received 26 June 2008; published 8 October 2008)

Various experimental settings that involve drying solutions or suspensions of nanoparticles—often called nanofluids—have recently been used to produce structured nanoparticle layers. In addition to the formation of polygonal networks and spinodal-like patterns, the occurrence of branched structures has been reported. After reviewing the experimental results we use a modified version of the Monte Carlo model first introduced by Rabani *et al.* [Nature **426**, 271 (2003)] to study structure formation in evaporating films of nanoparticle solutions for the case that all structuring is driven by the interplay of evaporating solvent and diffusing nanoparticles. After introducing the model and its general behavior we focus on receding dewetting fronts which are initially straight but develop a transverse fingering instability. We analyze the dependence of the characteristics of the resulting branching patterns on the driving effective chemical potential, the mobility and concentration of the nanoparticles, and the interaction strength between liquid and nanoparticles. This allows us to understand the underlying instability mechanism.

DOI: [10.1103/PhysRevE.78.041601](https://doi.org/10.1103/PhysRevE.78.041601)

PACS number(s): 68.08.Bc, 61.46.Df, 47.20.Hw, 05.10.Ln

I. INTRODUCTION

Branched structures are ubiquitous in nature. They appear in a wide variety of phenomena including growing trees, river networks, dendrites in solidification, and crystallization [1]. In hydrodynamical systems they occur, for instance, in Saffmann-Taylor fingering [2] whose zero-interface-tension limit is well described by the discrete computational model of diffusion-limited aggregation [3]. Branched patterns may also result from contact line instabilities in spreading drops of surfactant solution [4–6]. This is, however, rather an exception as in most cases transverse instabilities of advancing or receding contact lines do not lead to branched structures. Normally one finds either (i) arrays of straight parallel or wedge-shaped advancing fingers, as for a gravitationally driven front moving down an incline or vertical wall [7–11] or driven by thermal gradients [12–14]; (ii) fingers that advance radially outward in the case of a spinning drop [15]; or (iii) fingers [16–18] or fields of droplets [16,19–21] remaining at rest behind a receding circular or straight dewetting front (see also Sec. III of Ref. [22]).

For the presently studied system of an evaporating solution of gold nanoparticles that dewets a silicon substrate [23–27], fingering was predicted [28] using a kinetic Monte Carlo approach [26,29,30]. Recent experiments reviewed below in Sec. II have found such instabilities, analyzed their dependence on the properties of the nanoparticles, and could furthermore justify the usage of the seemingly simplistic Monte Carlo model [31]. This will be elucidated in more detail below in Sec. III A.

In the broader field, dewetting experiments with evaporating suspensions of particles or macromolecules

are performed by various groups in a wide variety of settings. Examples include drying macroscopic drops of colloidal solutions of micrometer- or nanometer-sized particles [32–36], spin-cast aqueous collagen solutions [37–39], spin-cast solutions of polystyrene in benzene [40], and spin-cast solutions of polyacrylic acid in toluene [41]. The behavior presented in these studies is generic for a wide class of solvents and solutes (see, e.g., the references in [40]). More complex situations have also been studied, such as evaporating thin films of a binary polymer solution on horizontal [42] or inclined [43] substrates, a drying binary suspension of hard-sphere colloidal particles and a nonadsorbing polymer [44], and structuring of polymer solution films caused by high-temperature evaporation or boiling in a dip-coating setting [45,46].

For less complex systems, in several regions of the parameter space, the dewetting behavior of the solutions appears to be very similar to that described for simple polymeric liquids [22,47–49]. In these regions it is possible to use the solute to “image” the dewetting patterns created by the volatile solvent. This route was taken, for example, in Refs. [37,39]. This is, however, not the case in other parameter regions. Most strikingly, the experiments show that dewetting (evaporating) solutions show much stronger transverse instabilities of the dewetting front than pure liquids (see, e.g., Refs. [31,41,50]).

The present paper focuses, after a short review of the experiments (Sec. II), on an analysis of the fingering instability employing the kinetic Monte Carlo model as developed in Ref. [29] and later modified in [26]. Section III introduces the model and the numerical algorithm. Section IV reviews the general behavior of the model, whereas Sec. V entirely focuses on a parametric analysis of the fingering instability. Finally, Sec. VI concludes and gives an outlook for future work.

^{*}vancea@mpipks-dresden.mpg.de

[†]u.thiele@lboro.ac.uk; <http://www.uwethiele.de>

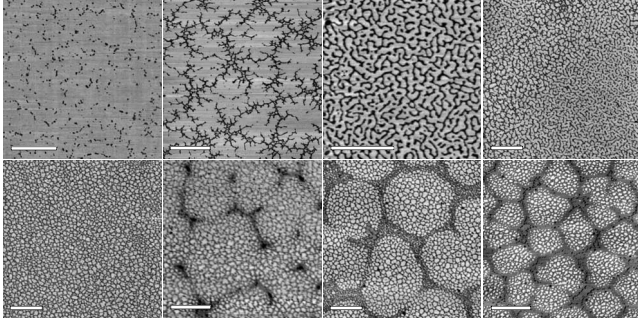


FIG. 1. AFM images of dodecanthiol-passivated 2 nm gold nanoparticles, spin-coated from toluene onto native-oxide-terminated silicon substrates. From top left to bottom right, concentrations increase as follows: 0.10, 0.25, 0.50, 0.75, 1.00, 1.25, 1.50, and 1.75 mg/ml. Scans are 2×2 to $5 \times 5 \mu\text{m}^2$ in size. All scale bars correspond to $1 \mu\text{m}$. The empty substrate is white, the deposited nanoparticles black.

II. EXPERIMENTS

In the following, we review recent experiments that use monodisperse colloidal solutions of thiol-passivated gold nanoparticles, sometimes called a “nanofluid.” The 2–3 nm gold core is covered by alkyl-thiol molecules, whose carbon chain length can be changed from C_6 to C_{12} [31]. Variation of the length of the chain allows control of the interaction parameters, to a certain extent. In general, the particles are hydrophobic and are then easily suspended in toluene. They can also be made hydrophilic by modifying the termination of the passivating alkyl-thiol molecules. Then they can be suspended in water or in another polar solvent. Most experiments are carried out using hydrophobic particles. Normally, the solution is deposited (see below) on a silicon substrate that is covered only by the native silicon oxide layer [25]. However, the wetting behavior of the solvent (and the interaction of the nanoparticles with the substrate) can be (locally) changed by oxidizing the substrate further [27]. The properties of the solvent can be changed as well, e.g., by adding excess thiol (which is thought to mainly affect the viscosity of the solution [31]).

The actual deposition process is very important to determine evaporation speed and, in consequence, the results of the ongoing pattern formation process. Two procedures are followed. On the one hand, a thin film of solution is deposited by spin-coating a drop of solution onto the native-oxide-terminated silicon substrate. Then evaporation competes with dewetting as was described some time ago in Ref. [39] for a related system involving a solution of macromolecules. After all of the solvent has evaporated, the resulting nanoparticle deposits are imaged using atomic force microscopy (AFM). Depending on the concentration of the solution, one may find mono- or bimodal cellular network structures as in Ref. [25], ribbonlike or labyrinthine structures, or branched structures (see Fig. 1). Flowerlike branched structures are also observed (Fig. 2). Note that for spin-coated films the evaporation is fast and normally the structuring is complete even before the spin-coater is stopped. At present, structuring of the film under spin-coating conditions has not been observed *in situ*.

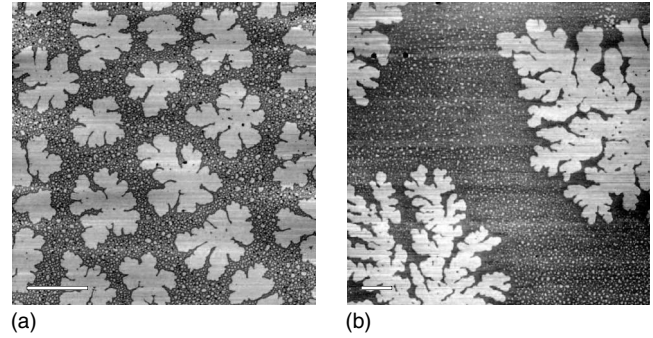


FIG. 2. AFM pictures of flowerlike branched structures in the case of (a) a toluene solution of gold nanoparticles spin-coated onto native-oxide-terminated silicon substrates, and (b) a toluene solution (with an excess of thiol) deposited using the meniscus technique. The empty substrate is white, the deposited nanoparticles black. Scale bars correspond to $2 \mu\text{m}$.

A meniscus technique using a Teflon ring was recently introduced [51] to decrease the solvent evaporation rate during nanoparticle self-organization. Precursors of this technique have involved the use of latex beads (see, e.g., Ref. [52] and references in Ref. [51]). The slowing down of the evaporation process improves control and allows the use of contrast-enhanced microscopy [53] to capture the dewetting process on video [31]. In the meniscus technique, a drop of solution is deposited into a Teflon ring that sits on the silicon substrate. As the toluene wets the Teflon, it evaporates quickly (within seconds) from the center of the ring only. The meniscus thereby formed between the silicon substrate and the Teflon ring slowly shrinks due to evaporation on the time scale of minutes to hours. The pattern formation process is confined to the region of the receding toluene/silicon/air contact line.

Using the meniscus technique one can observe (as for the spin-coating procedure) labyrinthine spinodal structures and mono- or bimodal network patterns depending on the nanoparticle concentration and position inside the Teflon ring. The position within the ring is closely linked to the solvent evaporation rate (for details, see Ref. [51]). It therefore becomes possible to study branched structures in a more controlled manner. Selected examples of such structures are given in Fig. 3. The systematic study performed in Ref. [31] indicates two important effects: Fingering strongly depends (i) on the chain length of the thiol molecules passivating the gold core of the particles and also (ii) on the amount of excess thiol in the solution. The chain length is varied from pentane (C_5) to tetradecane (C_{14}) at fixed nanoparticle concentration and deposited volume [see Figs. 2(a)–2(e) of Ref. [31]]. For C_5 and C_8 ligands, no formation of branched structures is observed irrespective of evaporation rate, i.e., position within the Teflon ring. For longer chains (C_{10} and C_{12}) well-developed branched structures are formed. Increasing the chain length even further (C_{14}), however, produces less developed branching. An addition of a small amount of excess thiol to the solution (0.1% by volume) enhances the development of branched structures strongly (see Ref. [31]). For small chain length (C_5 and C_8) branching (albeit sometimes weak) is now observed. The branching is considerably stronger for C_{10} , C_{12} , and C_{14} .

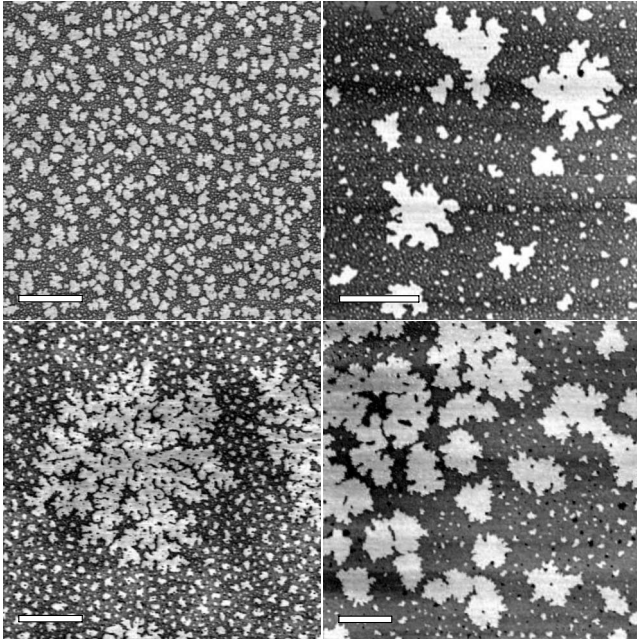


FIG. 3. AFM pictures of fingering patterns obtained by evaporative dewetting using the meniscus technique. The employed thiol-passivated gold nanoparticles are coated with thiol molecules of different lengths. Shown are images representative of chain length from top left to bottom right (a) C_8 , (b) C_{10} , (c) C_{12} , and (d) C_{14} . No excess thiol is present. The empty substrate is white, the deposited nanoparticles black. Scale bars correspond to $1 \mu\text{m}$.

The main aim of the present work is to shed more light on the mechanisms underlying the branching process using a simple computational model [26,29]. To separate the process from other effects, we analyze the dependence of the branching of a straight evaporative dewetting front on the control parameters. The results are used to explain the experimental findings and indicate avenues for future experiments. We will come back to this below in the Conclusions.

III. KINETIC MONTE CARLO MODEL

A. Justification of usage

A simple two-dimensional kinetic Monte Carlo model for the present process was first proposed in Ref. [29] to model experiments such as those presented in Ref. [24]. Before we introduce the model in detail, we first discuss its applicability and justify its usage. The model is based on two key assumptions: (1) that the relevant processes can be captured by a two-dimensional setting neglecting changes in the film thickness of the evaporating film; and (2) that all relevant dynamics are a result of the diffusion of nanoparticles and of the evaporation of the solvent. Convective motion of the solution is entirely neglected. A refined model increases the spatial range of the energetic interactions including next-nearest neighbors [26] but otherwise uses the same basic assumptions. Considering the strong assumptions, the agreement with experiments is amazingly good [26,29]. As we shall now discuss, recent experiments using the meniscus technique (described above) may explain why.

In Ref. [31] the evolution of the branched patterns is followed in real time using contrast-enhanced video microscopy. The video (complementary material of Ref. [31]) clearly shows that different processes occur on different scales. First, a macroscopic dewetting front recedes, leaving behind a seemingly dry substrate. The macroscopic front can be transversely unstable, resulting in large-scale ($>100 \mu\text{m}$) strongly anisotropic finger structures. For fronts that move relatively quickly these macroscopic structures cover all available substrate. However, when at a later stage the macroscopic front becomes slower, those fingers become scarce and “macroscopic fingering” finally ceases. At this stage it is possible to appreciate that the seemingly dry region left behind by the front is not at all dry, but covered by an ultrathin “postcursor” film that is itself not stable. At a certain distance from the macroscopic front the ultrathin film starts to evolve a locally isotropic pattern of holes. The holes themselves grow isotropically in an unstable manner, resulting in an array of isotropically branched structures as shown, e.g., above in Figs. 2 and 3. This indicates that nearly all of the patterns described in various publications result from processes in the ultrathin film whose thickness is of the order of the size of the nanoparticles.

Focusing on the structuring of the ultrathin film, we next identify the important dynamical processes. On the mesoscopic scale the dynamics of a thin film of pure liquid can be described by a thin film equation derived using a long-wave approximation [54,55]. In such a model, the temporal change in film thickness h results from the gradient of the convective flow $h^3(\nabla p)/3\eta$ and from an evaporative loss $\beta(\rho\mu_0 - p)/\rho$ [56,57]. Here, η and ρ are the dynamic viscosity and density of the solvent, respectively, μ_0 is the chemical potential (related to the ambient vapor pressure of the solvent), and β is a rate constant that can be obtained from gas kinetic theory or from experiment [56]. The pressure p contains curvature and disjoining pressures and drives both processes—convection and evaporation. The disjoining pressure describes the wettability of the substrate [22,47,58,59]. Due to the thickness dependence h^3 , the mobility related to convective motion is large for thick films but decreases strongly with decreasing film thickness, whereas the mobility related to evaporation (the rate constant) is a constant. In consequence, it is expected that for a nanometric film the evaporation term strongly dominates. Using the parameters given in Ref. [56] and assuming a small contact angle of about 0.5° , one obtains a crossover thickness in the lower-single-digit nanometer range. Below this thickness the solvent dynamics is dominated by evaporation.

This consideration, together with the experimental observation discussed above, justifies the neglect of convective motion in the kinetic Monte Carlo model. Without convection a two-dimensional model is sufficient to cover the essential processes. Note that a refinement proposed in [27] introduces a three-dimensional aspect into the two-dimensional model by making the chemical potential dependent on mean liquid coverage (i.e., on a parameter related to mean thickness). This amounts to a consideration of the thickness-dependent disjoining pressure in the evaporation term *without* the explicit incorporation of a film thickness. The resulting pseudo-three-dimensional model successfully

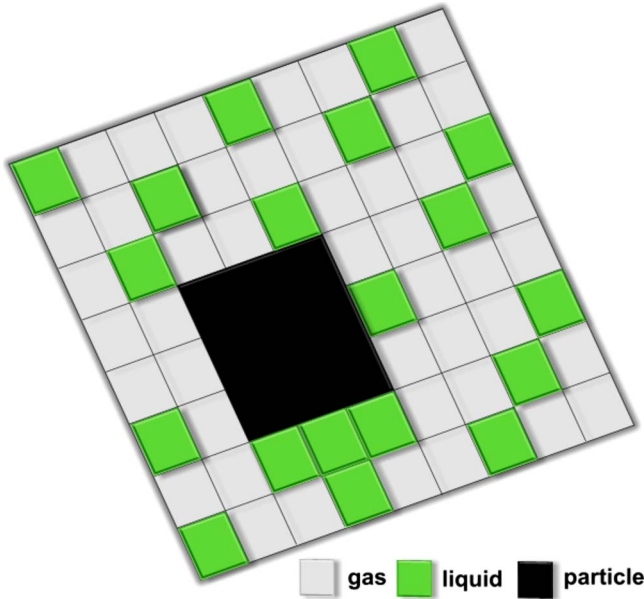


FIG. 4. (Color online) Schematic picture of the two-dimensional lattice gas model used: the size of nanoparticles is in our case 3×3 , whereas a liquid cell is of size 1×1 . The side length of such a cell represents the correlation length of the solvent approximated to be 1 nm [29].

reproduces bimodal structures [27,60]. These will, however, be of no concern here.

B. The model

Kinetic Monte Carlo models are a common tool to investigate a wide variety of dynamical processes [61,62]. In particular, they are attractive tools to model adsorption, diffusion, and aggregation in surface science resulting in interfacial growth and structuring such as, e.g., the growth of metal layers as atoms arrange after being deposited on surfaces [63–65].

The approach followed in Ref. [29] to model an evaporating dewetting nanoparticle solution is based on an Ising-type model for the liquid-gas phase transition. To facilitate comparison with previous work, we here choose the model to be exactly the same as in Ref. [26] (building on Ref. [29]): The system is described using a two-dimensional lattice gas of two fields n and l . We allow for three types of possible states of a cell—liquid ($l=1, n=0$), nanoparticle ($l=0, n=1$), and vapor ($l=0, n=0$, i.e., cell empty). Thereby liquid or vapor is assigned per 1×1 cell whereas it is assumed that the nanoparticles fill 3×3 cells (see the sketch in Fig. 4) to indicate the larger size of the nanoparticles used in the experiment as compared to the correlation length of the liquid. This detail, however, turns out to be not very relevant as further discussed in the Conclusions.

The energy of a configuration of the two-dimensional assembly of vapor, liquid, and nanoparticles is determined by the Hamiltonian

$$E = -\frac{\varepsilon_{nn}}{2} \sum_{\langle ij \rangle} n_i n_j - \frac{\varepsilon_{nl}}{2} \sum_{\langle ij \rangle} n_i l_j - \frac{\varepsilon_{ll}}{2} \sum_{\langle ij \rangle} l_i l_j - \mu \sum_i l_i, \quad (1)$$

where ε_{ll} , ε_{nn} , and ε_{nl} are the interaction energies for adjacent sites (i, j) filled by (liquid,liquid), (nanoparticle,nano-

particle) and (liquid,nanoparticle), respectively. For fixed interaction strengths, the equilibrium state is determined by the chemical potential μ that controls the evaporation and condensation of the liquid. Note that μ is an effective potential that contains the thermodynamic chemical potential and, in addition, any wetting interaction of the solvent with the substrate, i.e., it contains a contribution of an “overall disjoining pressure.” It does not, however, distinguish between different short- and long-range components of the disjoining pressure. This can be done in a pseudo-three-dimensional model by making μ dependent on liquid coverage (cf. [27,60]). Note, furthermore, that there is no parameter that accounts for the affinity of the particles to the substrate as it would not have any influence in a two-dimensional model for a homogeneous substrate. Compare, however, Ref. [27], where such a term is included to account for spatial heterogeneity.

We will call $|\mu|$ the driving force as it is primarily responsible for the motion of a dewetting or wetting front. The sums $\sum_{\langle ij \rangle}$ are taken over all pairs of nearest and next-nearest neighbors. Thereby, the interaction strength of the next-nearest neighbors is corrected by a factor $1/\sqrt{2}$ due to their larger distance [26]. In the following we fix $\varepsilon_{ll}=1$, i.e., we express all energies and the chemical potential in the scale of the liquid-liquid interaction energy.

The energy functional determines the equilibrium state and the energy landscape of the system. The dynamics is determined by the allowed Monte Carlo moves, their relative frequency, and the rules for their acceptance. Two types of moves are allowed: (i) evaporation or condensation of liquid and (ii) diffusion of nanoparticles within the liquid. To simulate the dynamics, the energy loss or gain ΔE related to a potential move is calculated. The move is then accepted with the probability $p_{\text{acc}} = \min[1, \exp(-\Delta E/kT)]$ where k is the Boltzmann constant and T the temperature. The rule implies that any move that decreases the energy of the system is accepted when tried. Any move that increases the energy has a probability corresponding to the related Boltzmann factor. Consistent with the above scales, temperature is expressed in units of ε_{ll}/k . It determines the importance of fluctuations in the system. For $T=0$ the system is fluctuation-free, i.e. the evolution follows a deterministic gradient dynamics.

Practically, we use a checkerboard Metropolis algorithm to advance the liquid-vapor subsystem; each solvent or vapor cell is examined in turn, and is converted from liquid to vapor or from vapor to liquid with the acceptance probability p_{acc} . After one solvent cycle all particles are considered and a diffusive move is tried. The nanoparticles are free to perform a restricted random walk on the lattice. It is restricted because particles are only allowed to move into wet areas of the substrate, i.e., onto cells with $l=1$. This is a very important rule and models zero diffusivity of the particles on a dry substrate. If such a “forbidden” move is tried, the particle is left at rest and the next particle is considered. The diffusivity or mobility of the nanoparticles inside the liquid is controlled by the number of times each particle is examined after one solvent cycle. This computational ratio M of particle and solvent cycles reflects the physical ratio of time scales for evaporation and diffusion. Large M , for instance, indicates that diffusion is fast as compared to evaporation, i.e., it stands for a large diffusion constant of the nanoparticles

or/and a low evaporation rate for the liquid. It therefore represents a low effective viscosity of the solution.

The model is used in the following to first review some general results for a homogeneous system without and with nanoparticles (Sec. IV). Then we focus on a parametric analysis of the fingering instability (Sec. V).

IV. BEHAVIOR OF A HOMOGENEOUS SYSTEM

A. Without nanoparticles

Without nanoparticles the behavior of the model introduced in Sec. III is well known as it reduces to the classical Ising model in two dimensions describing the order-disorder transition in a ferromagnetic system. Using the mapping $\mu \rightarrow \mu_0 H - 2$ and $l \rightarrow (s+1)/2$, where $s = \pm 1$ corresponds to the spin of a cell, μ_0 to the magnetic moment, and H to the external magnetic field, all results since Onsager [66] can be used. In particular, an infinitely extended system has a critical point at $\mu_c = -2$ and $kT_c^\infty = 1/[2 \ln(1 + \sqrt{2})] \approx 0.567$. For temperatures below T_c^∞ at $\mu_{\text{ph}} = -2$ the liquid state and the vapor state may coexist, whereas for $\mu < -2$ ($\mu > -2$) eventually the vapor (liquid) state dominates. A chemical potential not equal to -2 corresponds to a nonzero external magnetic field in the ferromagnetic system.

For $T < T_c^\infty$ there exists a first-order phase transition at μ_{ph} ; systems in the liquid (gas) state are metastable for a certain range below (above) μ_{ph} . Mean field theory as presented, e.g., in Ref. [67], provides the line that is the lower (upper) limit for the existence of metastable liquid (gas) states in the (μ, kT) plane. The two curves satisfy

$$\mu_{\text{ms}}^\pm = \pm \frac{2}{3} kT \left(\frac{T_c^\infty}{T} - 1 \right)^{3/2} - 2, \quad (2)$$

where we set the grid spacing used in Ref. [67] to 1.

An overview of the equilibrium phases and the resulting behavior of a straight wetting-dewetting front (as described next) is given in Fig. 5. Starting with a liquid-covered substrate in a region ($\mu < -2$) where the global energy minimum corresponds to the vapor phase leads to an evaporative dewetting process that either follows a nucleation and growth pathway or results from a spinodal-like process. Typical snapshots illustrating the occurring processes are shown in Fig. 6. Nucleation and growth of holes occur in the parameter region close to $\mu_{\text{ph}} = -2$ where the homogeneous liquid state is still metastable. At smaller $\mu < \mu_{\text{ms}}^-$, i.e., at larger driving forces $|\mu|$, a spinodal-like process occurs when we start with a liquid-filled plane. Many very small holes appear at once, and all liquid evaporates very quickly, leaving the substrate empty. When starting with a homogeneous gas state at $\mu > -2$, similar mechanisms result in a liquid-filled plane. The relevant border there is $\mu = \mu_{\text{ms}}^+$.

A straight front separating vapor- and liquid-covered substrate areas remains on average at rest for $\mu = -2$ although it might fluctuate quite strongly. The liquid state will advance and recede for $\mu > -2$ and $\mu < -2$, respectively. For a resting or moving front the temperature ($T < T_c$) determines the strength of the fluctuations that modulate the straight front (see snapshots at the right of Fig. 5). The overall picture is

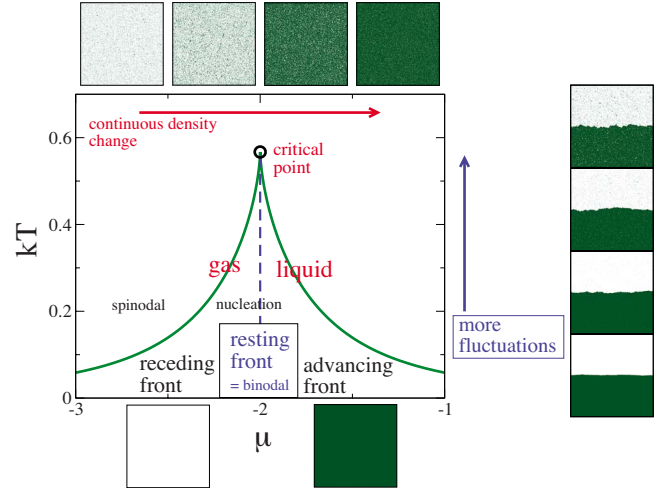


FIG. 5. (Color online) Phase diagram without nanoparticles (central panel). A schematic overview of system behavior is given in the plane spanned by the dimensionless chemical potential μ and the dimensionless measure of temperature kT . The liquid and gas phases are indistinguishable above the critical temperature $kT_c = 1/[2 \ln(1 + \sqrt{2})] \approx 0.57$. The corresponding gradual change of mean density with μ is indicated by the four snapshots of equilibrium states shown in the upper line (from left to right: $\mu = -2.75, -2.25, -1.75, \text{ and } -1.25; kT = 0.8$). Below T_c the system can show a rich dynamics when evolving toward equilibrium. For $\mu > -2$ ($\mu < -2$) the equilibrium corresponds to liquid (gas) as illustrated by the snapshots in the bottom row [$\mu = -1.5$ ($\mu = -2.5$) and $kT = 0.05$], whereas at $\mu_{\text{ph}} = -2$ gas and liquid may coexist. At μ_{ph} a straight front separating gas and liquid does not move on average. However, depending on temperature, it fluctuates, as illustrated by the snapshots in the right column (from bottom to top $kT = 0.1, 0.3, 0.45, \text{ and } 0.55; \mu = \mu_{\text{ph}} = -2$). A straight liquid front will recede (advance) for $\mu < -2$ ($\mu > -2$), i.e., one is able to study evaporative dewetting (wetting) fronts. Starting, however, with a homogeneous liquid-covered (gas-covered) substrate for $\mu < -2$ ($\mu > -2$), the substrate will empty (fill) via a nucleation or spinodal-like process. The borders between the different processes are indicated as heavy lines and are discussed in the main text. All snapshots are obtained from simulations for a small domain size of 300×300 after 1000 kinetic Monte Carlo steps.

similar for circular fronts, however, the exact value of μ that results in a resting front depends on the average curvature of the front (i.e., the size of the hole). A two-dimensional “curvature pressure” enters the balance. Fixing some $\mu_{\text{ms}}^- < \mu < -2$, a hole in a liquid layer will grow (shrink) above (below) a certain radius $r_c(\mu)$. The growing hole will remain almost circular. Practically, on a square grid in late stages it will become squarelike (the original model in Ref. [29] where only nearest neighbors are considered). Including next nearest neighbors leaves the holes circular up to a later stage, when they become octagonal.

B. With nanoparticles

Having discussed the behavior of the model without particles, we now turn our attention toward situations where nanoparticles are present. First, we discuss the equilibrium

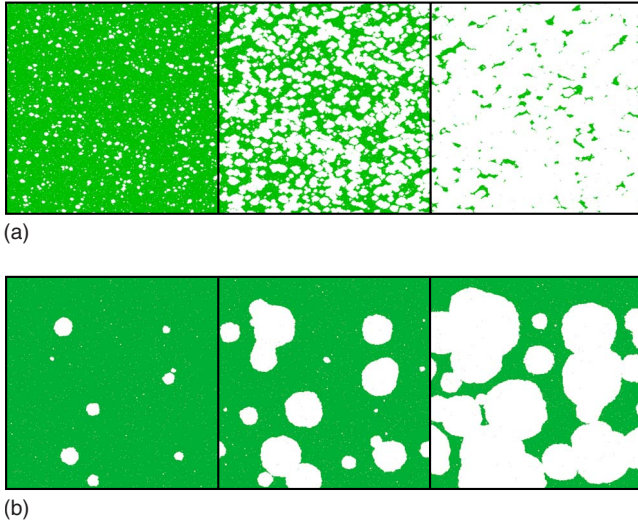


FIG. 6. (Color online) Snapshots from typical evaporative dewetting processes without nanoparticles in the case of (a) a spinodal-like process at $\mu = -2.55$ and (b) nucleation and growth of holes at $\mu = -2.3$. The starting condition in each case is a homogeneous liquid film. The number of Monte Carlo steps is from left to right (a) 5, 10, and 15; (b) 40, 80, and 120; $kT = 0.3$ and the lattice size is 600×600 . Liquid is gray (green online) and the empty substrate is white.

behavior, followed by an analysis of the evolution of an initially liquid-filled well-mixed homogeneous system.

We expect the particles to influence the location of the liquid-gas phase transition. Inspecting the Hamiltonian (1), one can estimate the influence using a mean-field argument. Let us consider a liquid-filled cell at a straight liquid front. We consider the energy needed to move the front, i.e., to empty the cell. On average a cell at a straight front has two direct neighbors occupied by either liquid or nanoparticles. We replace the nanoparticle occupation number in the liquid-particle interaction term by its mean value, i.e., the coverage ϕ , neglect the particle-particle interaction term as we consider a cell filled by either liquid or gas, and replace one of the liquid occupation numbers in the liquid-liquid interaction term by its mean value for a filled cell, $1 - \phi$. In this way we can map the model onto the pure liquid-gas case by replacing μ by $\tilde{\mu} = \mu + 2(\epsilon_{nl} - 1)\phi$. Following this argument we expect the phase transition to occur at $\tilde{\mu} = -2$, i.e., an attractive liquid-gas interaction ($\epsilon_{nl} > 0$) stronger than the liquid-liquid interaction ($\epsilon_{ll} = 1$) implies that the phase transition occurs at $\tilde{\mu}_{ph} = -2 - (\epsilon_{nl} - 1)\phi < \mu_{ph}$. Note, however, that for low particle concentrations (e.g., $\phi = 0.1$) the change is rather small for $\epsilon_{nl} = 1.5$, i.e., the value used in most of the present work. This agrees with simulations, where we have not spotted a significant shift for the used concentrations ≤ 0.2 .

The aspect that most interests us here is, however, not the equilibrium behavior but the dynamics of the liquid-gas phase transition. As in Sec. IV A we start at a $\mu < -2$ with a liquid-covered substrate, i.e., in a region where the final state without nanoparticles corresponds to the vapor phase. Now, however, although the liquid evaporates the nanoparticles remain. Depending on the particular parameter values chosen, one finds final structures that do not change any more on

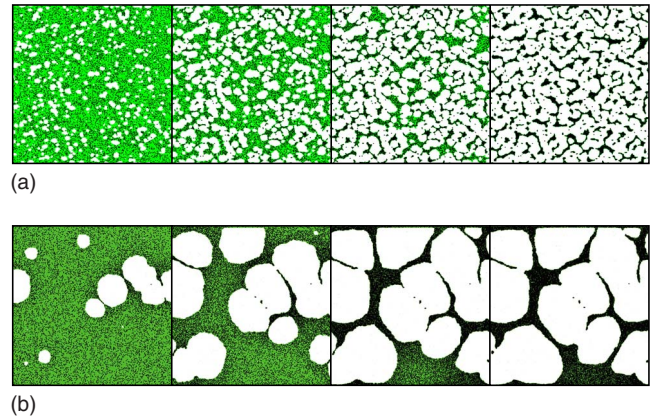


FIG. 7. (Color online) Snapshots from typical evaporative dewetting processes with nanoparticles in the case of (a) a spinodal-like process at $\mu = -2.55$ and (b) nucleation and growth of holes at $\mu = -2.3$. Starting condition: homogeneous liquid film with homogeneously distributed particles. The number of Monte Carlo steps is indicated in the individual panels (top, 10, 15, 20, 100, bottom, 100, 200, 300, 400); $\epsilon_{nl} = 2$, $\epsilon_{nl} = 1.5$, $M = 50$, $\phi = 0.2$. The remaining parameters are as in Fig. 6. Particles are black, liquid is gray (green online), and empty substrate is white.

short time scales. They might, however, slowly evolve, e.g., by coarsening on long time scales as conditions are “fluxional” [29]. The final dried-in structures depend on the pathway of evaporative dewetting (i.e., on kT , μ , the interaction constants ϵ_{ij} , nanoparticle concentration ϕ , and mobility M) and range from labyrinthine to polygonal network structures or holes in a dense particle layer. Typical snapshots from the evolution of a layer of solution are shown in Fig. 7. As before, the evaporative dewetting process of the solvent follows either a nucleation and growth [Fig. 7(b)] or a spinodal-like [Fig. 7(a)] pathway. Following the mean-field argument as above we expect for the limiting curve $\mu_{ms}(kT)$ separating the two processes in the parameter plane again a shift by $-2(\epsilon_{nl} - 1)\phi$. However, due to fluctuations this border is elusive when scrutinized numerically; therefore we will not try to compare simulations to the prediction. This is similar to the occurrence of instability- and nucleation-dominated regimes inside the spinodally unstable parameter range for dewetting nonvolatile films as discussed in Refs. [22,68,69] using a lubrication model. There the size of defects (strength of noise) determines which process will dominate.

At first sight, however, one might get the impression that the particles act as a type of passive tracer that preserves the transient volatile dewetting structures of the solvent. This idea was put forward in Refs. [37–39] in the context of experiments on dewetting aqueous solutions of macromolecules and provides an explanation for some of the basic features of the observed network structures. One can also employ this hypothesis to explain some of the structures observed in the present study, such as the network and spinodal structures shown in Fig. 7. The simulations indicate, however, that the nanoparticles are not simply passive tracers. Although the particles primarily just follow the solvent, they play an important role in several phases of the process.

First, the particles may influence the nucleation process in the metastable parameter region, beyond the “shift” in μ pre-

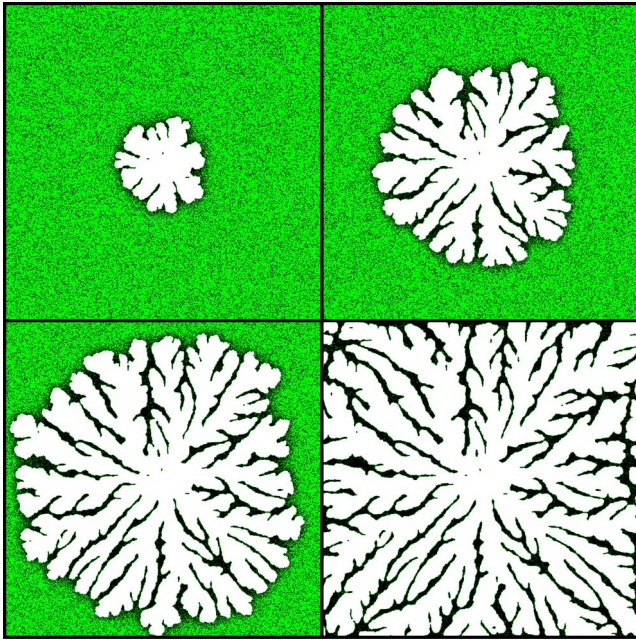


FIG. 8. (Color online) Snapshots illustrating the unstable growth of a nucleated hole in a film of nanoparticle solution. The strong branched fingering caused by the nanoparticles can be seen clearly. From top left to bottom right the number of Monte Carlo steps is 450, 1200, 1800, and 3000. Nanoparticle-related parameters are $\varepsilon_{nm}=2$, $\varepsilon_{nl}=1.5$, $\mu=-2.3$, $M=5$, $\phi=0.2$. The remaining parameters are as in Fig. 6. Particles are black, liquid is gray (green online), and empty substrate is white.

dicted by the mean-field considerations above. Although our simulations seem to indicate that the nucleation rates actually depend on the particles themselves, we cannot quantify the effect at present. We leave this question for future investigations and focus here on the second and more pronounced influence. Second, for a low mobility of the particles, i.e., for a slow diffusion of particles as compared to the evaporation of the solvent, the nucleated holes might grow in an unstable manner as illustrated in Fig. 8. The transverse instability of the dewetting front responsible for this effect is analyzed in more detail in the following section.

V. THE FINGERING INSTABILITY

A straight evaporative dewetting front in the absence of nanoparticles moves with a constant mean velocity \bar{v} (averaged over the transverse direction). The velocity depends only on the driving chemical potential. The local velocity, however, fluctuates with temperature. The fluctuations are illustrated in the column of snapshots at the right of Fig. 5. Therefore, the local front position also fluctuates around the steadily advancing or receding mean position. The velocity is easily measured numerically for driving forces small enough that the nucleation of additional holes is not very probable during the time of measurement. Here this is the case for $\mu \geq -2.4$. The dependency of \bar{v} on μ is given for comparison below in Fig. 12. One finds that the velocity increases linearly with the driving force.

Adding diffusing nanoparticles to the solvent changes the front behavior dramatically as it may become transversally unstable. Such an unstable front not only fluctuates around a continuously receding mean position but fingers stay behind permanently (for the front instability of a growing circular hole, see Fig. 8 above). To elucidate the underlying mechanism we will in the next sections discuss the influence of the individual system parameters on the instability, i.e., the influence of chemical potential μ , particle concentration ϕ , and mobility M .

For each dependency we present snapshots of the final dried-in nanoparticle structure corresponding to the dried-in patterns observed in experiment. We add, however, thin lines that correspond to positions of the dewetting front at equidistant times throughout the evolution. The final branched patterns we characterize in a rather simple but effective manner. We determine an averaged finger distance by dividing the side length of the computational square domain by the average finger number. The latter is obtained by counting the fingers on each line orthogonal to the mean direction of front motion (here the y direction) and averaging over the y range where fingers exist. The underlying hypothesis that the finger patterns are “stationary” will be discussed and checked below. Attempts to determine a mean distance of fingers employing a one-dimensional (1D) Fourier transform unfortunately did not give meaningful results because of the strong side branching (see snapshots below). Note that the finger number corresponds to a wave number rescaled by $2\pi/L$ where L is the side length of the computational domain (which is fixed throughout this section and corresponds to about $1.2 \mu\text{m}$).

A. Dependence on chemical potential

First, we focus on the influence of the driving force, i.e., the chemical potential. Fixing the particle concentration to $\phi=0.1$ and the mobility to $M=20$, the final structures observed for various values of μ are shown in Fig. 9, whereas Fig. 10 shows the dependence of the mean finger number on the chemical potential. The driving force increases for decreasing μ and the number of fingers increases roughly linearly. Again, for $\mu \leq -2.4$ nucleation becomes more probable and we observe a random polygonal network. The side branches of the polygonal pattern clearly result from the transverse instability [see Fig. 9(d)].

Further inspection of Fig. 9 results in the following observations.

(i) Both the wave number and the growth rate of the front instability increase with decreasing μ . A faster growth translates into longer fingers in the dried-in structure, i.e., fingers that extend further up in Fig. 9. Starting from the same initial front position, the fingers appear much earlier in Fig. 9(c) than in Figs. 9(b) and 9(a).

(ii) The front contours taken at equidistant times indicate that the front is already strongly disturbed before the instability becomes manifest in a deposited finger, i.e., parts of the front slow down before actually stopping (and depositing material). This is especially well visible in Fig. 9(a).

(iii) The dried-in fingering structure is not entirely frozen as the chosen parameter values are in a fluxional regime [29].

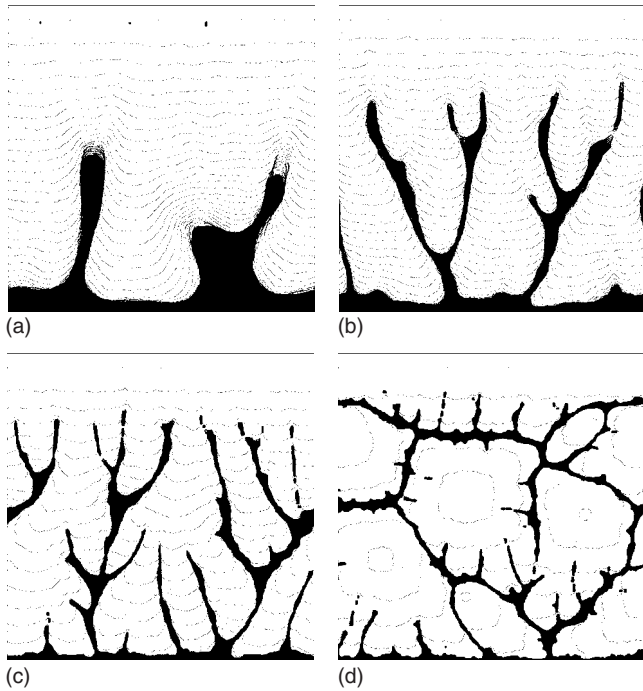


FIG. 9. Final dried-in branched fingering structure for evaporative dewetting of a nanoparticle solution for different driving forces, i.e., chemical potential $\mu =$ (a) -2.1 , (b) -2.2 , (c) -2.3 , and (d) -2.4 . Thin lines correspond to positions of the dewetting front at equidistant times with $\Delta t = 333$ (a) and 166 (b), (c), (d). The domain size is 1200×1200 , $M = 20$, $\phi = 0.1$, $kT = 0.2$, $\varepsilon_{nm} = 2$, and $\varepsilon_{nl} = 1.5$.

This is especially well visible at the tips of the fingers in Fig. 9(a), which continue to retract very slowly, or in Fig. 9(b), where a thin part of the rightmost finger breaks and slowly retracts as well. Eventually, this will lead to a long-time coarsening of the finger structure.

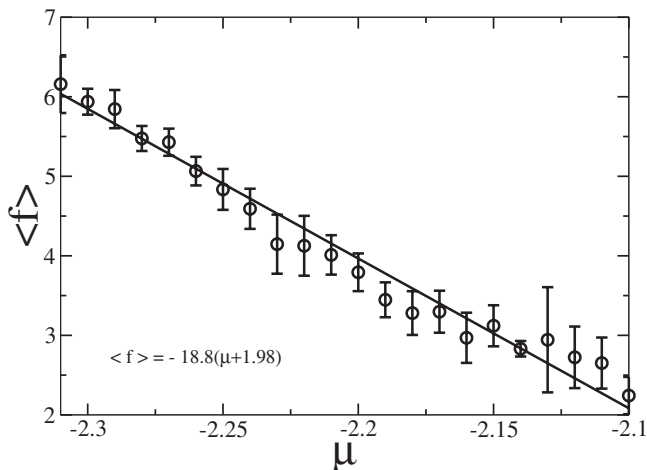


FIG. 10. Dependence of mean finger number $\langle f \rangle$ of the final dried-in structures (determined as described in the main text) on chemical potential μ . Every data point corresponds to the mean value of seven simulations; error bars indicate the corresponding standard deviation. The solid line corresponds to a linear mean-square fit with coefficients given in the plot. The remaining parameters are as in Fig. 9.

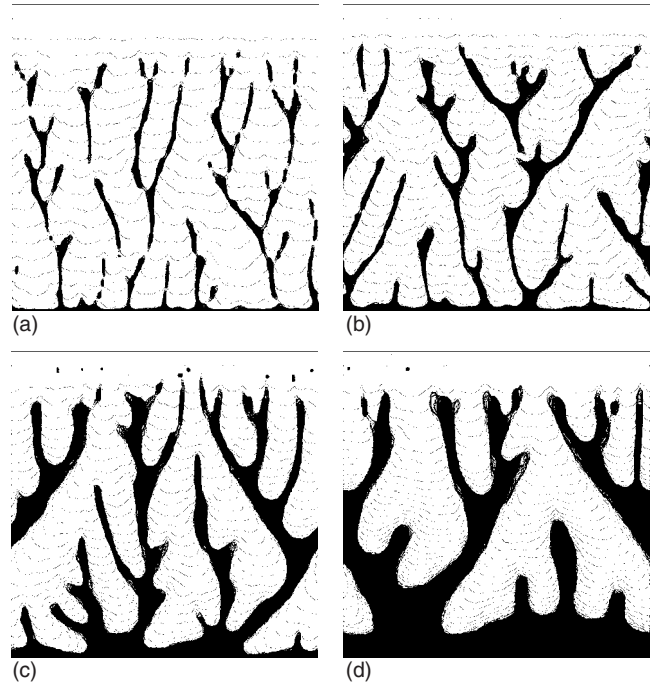


FIG. 11. Final dried-in branched fingering structure for evaporative dewetting of a nanoparticle solution for different nanoparticle concentration $\phi =$ (a) 0.05 , (b) 0.10 , (c) 0.20 , and (d) 0.30 . Thin lines correspond to positions of the dewetting front at equidistant times with $\Delta t = 166$ (a), (b), 333 (c), and 500 (d). The domain size is 1200×1200 , $M = 10$, $\mu = -2.2$, $kT = 0.2$, $\varepsilon_{nm} = 2$, and $\varepsilon_{nl} = 1.5$.

(iv) It is remarkable that even when fingers are left behind the local distance between consecutive front contours seems to be constant in each of the panels [apart from the regions discussed in (iii)]. One expects, however, that the front velocity depends on the local particle concentration and the mobility of the particles. The observation of a constant velocity indicates that the front instability is related to an auto-optimization of the front velocity. This is analogous to an effect described for dewetting polymer films [21]. There, a moving dewetting front “expels” part of the liquid rim and leaves the liquid behind in the form of deposited droplets. The instability avoids a slowing down of the dewetting front. Here, some of the particles that the evaporative dewetting front collects are expelled and deposited in fingers when too many are collected by the front.

Measurements of the front velocity for different μ and particle concentrations indeed show that the mean velocity is constant and depends linearly on μ (see Fig. 12 below).

B. Dependence on particle concentration

We have also examined the influence of the nanoparticle concentration ϕ on the fingering. Fixing the chemical potential at $\mu = -2.2$ and the mobility at $M = 10$, the final structures are shown for various values of ϕ in Fig. 11. From an initial inspection of Fig. 11 one might get the erroneous impression that the finger number increases with concentration. However, the statistics of many runs shows that the number is nearly independent of the particle concentration. The fingers

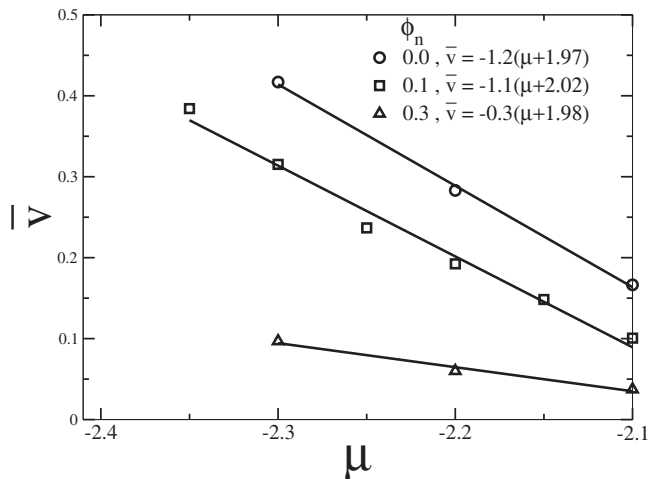


FIG. 12. Dependence of mean front velocity on chemical potential μ and for selected particle concentrations ϕ as given in the legend. The thin lines correspond to linear regression fits with coefficients as given in the plot. The used domain size is 1200×1200 , $M=20$, $kT=0.2$, $\varepsilon_{nn}=2$, and $\varepsilon_{nl}=1.5$. The velocity is averaged over 7000 Monte Carlo steps or the number of steps it takes to “dry” the substrate, whichever is smaller.

only become thicker with increasing concentration. This indicates that the fingering is controlled by the dynamical parameters responsible for the ratio of the time scales for diffusion of the particles and motion of the evaporative front (i.e., mobility and chemical potential). As the influence of the chemical potential has already been established in Sec. V A, we focus below in Sec. V C on the influence of mobility.

Before we do so we summarize in Fig. 12 results for the dependence of the global average front velocity on chemical potential and particle concentration. For all investigated concentrations the velocity decreases linearly with increasing chemical potential, i.e., with decreasing driving force. If we fix the chemical potential, the dewetting process is slower for higher particle concentrations. This implies that the finger number is not directly related to the mean front velocity, a result that will be discussed in the Conclusions.

C. Dependence on mobility

Fixing the particle concentration at $\phi=0.1$ and the chemical potential at $\mu=-2.2$, we show in Fig. 13 the final structures observed for selected values of mobility M . Figure 14 shows the dependence of mean finger number on mobility. One sees at once that mobility is very influential in the fingering process. For decreasing mobility of the particles the number of fingers increases strongly. As was observed for the influence of the chemical potential, the growth rate of the instability increases with increasing finger number, i.e., decreasing mobility. This is manifest in Fig. 13 by the later emergence of fingers for larger M , i.e., in the increasing distance of the finger tips from the upper domain boundary.

The systematic picture that emerges from the preceding three sections allows us to identify the primary factors influencing the fingering instability. It becomes obvious that they are of dynamical nature. Mobility is the major player. The

faster the nanoparticles can diffuse away from the dewetting front, the less likely the instability becomes as the front is not fast enough to “collect” the particles efficiently. This directly corresponds to the observation that the fingering becomes more intense with increasing driving force, i.e., lower chemical potential. Then the relative diffusivity is held constant (mobility M) but the mean front speed increases with decreasing μ . The greater the number of particles collected at the moving front, the more likely become lateral density fluctuations that lead to self-amplifying variations of the local front velocity. Note, however, that up to this point we kept all the interaction parameters ε_{ij} fixed. We expect them to influence the destabilizing feedback loop because, for example, a stronger particle-particle interaction ε_{nn} should support clustering. But one has to be cautious because the process is of dynamic character. Therefore it is difficult to predict whether a larger ε_{nn} implies fewer or more fingers. This question will be discussed below in Sec. V E.

Next, however, we will check the assumption of stationarity of the finger patterns that we have used above to introduce the measure of the mean finger number.

D. Stationarity of finger pattern

In Secs. V A–V C, we have used the mean finger number to characterize the parameter dependency of the fingering patterns. We noted that it represents a trustworthy measure only if the fingering process is stationary. By “stationary” we mean that the main properties of the pattern do not depend on the streamwise position. In other words, the moving dewetting front moves on average with a constant velocity and deposits on average the same amount of material in the same number of fingers.

To check this strong assumption we plot in Figs. 15 and 16 the dependence of finger number on the streamwise coordinate (y coordinate) for various values of the mobility and chemical potential, respectively. To smooth out fluctuations each curve represents the mean of 28 runs. As the fingers stay fixed after being deposited behind the front, an advance in y also indicates passing time. We note in passing that all “snapshots” above that show dried-in final structures can as well be read as space-time plots tracking the particle deposition at the moving dewetting front. Inspecting the curves, we note that they have some properties in common: (i) the finger number starts from zero at some value $y=y_s$ well behind the initial position of the front at $y=60$; (ii) the finger number grows exponentially on a typical length scale related to the (linear) growth rate of the fingering instability; (iii) a maximal finger number is reached before the number decreases again and settles onto a stationary level. The decay corresponds to a small coarsening of fingers and can be seen in several of the snapshots above. (iv) Fluctuations around the stationary level are small, i.e., on average as many new fingers are created (branch tips in the final image) as vanish when fingers join pairwise (at the branching points).

Our conclusion is that the mean finger number as used above is a valid measure because the y range where the initial overshooting occurs is relatively small, and also the overshoot itself is normally below 20% of the mean stationary

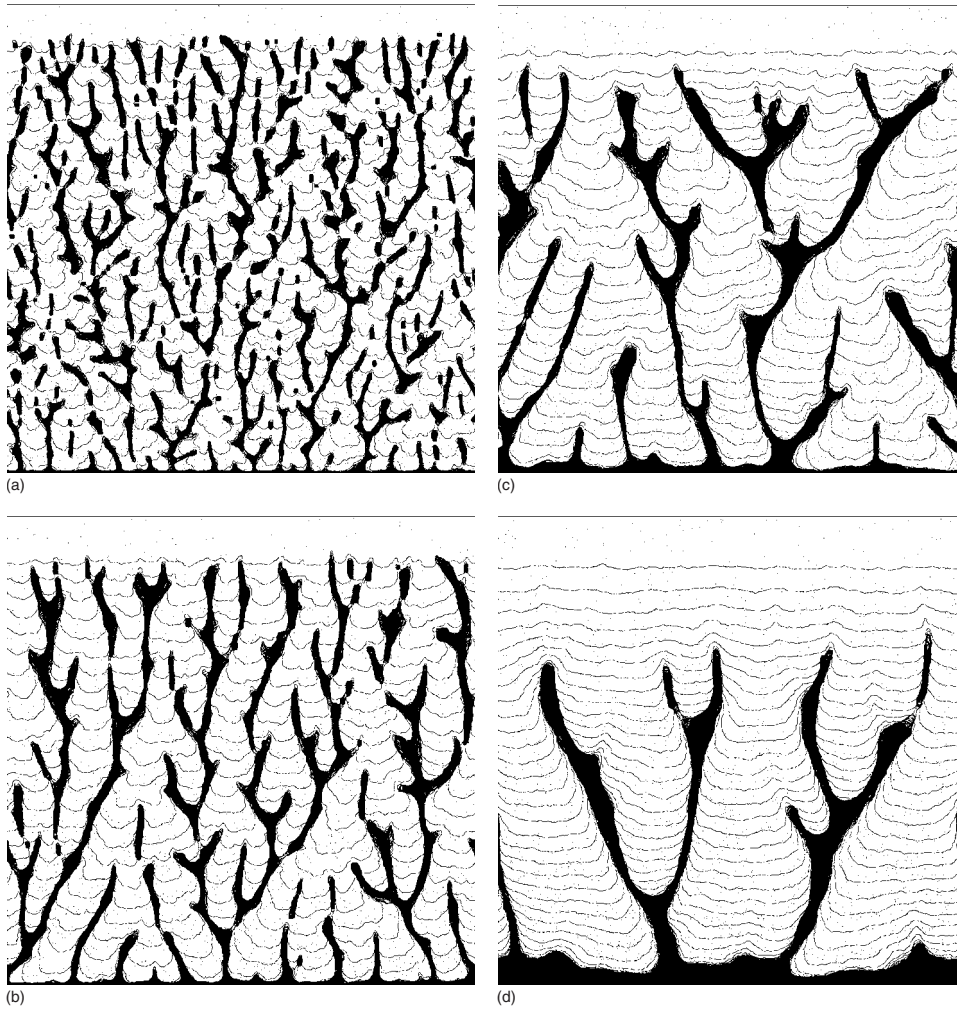


FIG. 13. Final dried-in branched fingering structure for evaporative dewetting of a nanoparticle solution for different nanoparticle mobilities $M=(a) 2$, $(b) 5$, $(c) 10$, and $(d) 20$. Thin lines correspond to positions of the dewetting front at equidistant times with $\Delta t=166$. The domain size is 1200×1200 , $\phi=0.1$, $\mu=-2.2$, $kT=0.2$, $\epsilon_{nn}=2$, and $\epsilon_{nl}=1.5$.

value. The resulting error is small as compared to the natural variance that we found between different runs. Note, however, that for several curves in Fig. 16 the decay after the initial maximum is relatively slow and the stationary value is not reached for our system size. This corresponds to a very slow coarsening of fingers as the front recedes.

E. Influence of interaction parameters

We mentioned in Sec. IV the hypothesis (put forward in [39] for a related system) that the ongoing pattern formation and the properties of the receding dewetting front mainly result from the dynamics of the liquid-gas phase transition. The nanoparticles were seen as passive tracers. This describes well the situation in the spinodal regime (taking into account that the mean-field parameters are slightly changed by the particles). We then showed that this picture has to be amended because the particles have an important influence during crucial phases of dewetting. Most notably, they are solely responsible for the transverse instability of the dewetting front leading to the branched finger patterns analyzed in detail in the present section.

The analysis up to now has been performed by fixing the interaction parameters ϵ_{ij} at convenient values: the liquid-liquid interaction serves as an energy scale, i.e., $\epsilon_{ll}=1$; the

particles attract each other slightly more than particles attract liquid ($\epsilon_{nn}=2$, $\epsilon_{nl}=1.5$). This ensures that particle-liquid phase separation does not generally occur in the bulk solution, but also that particle clusters are likely to form at higher

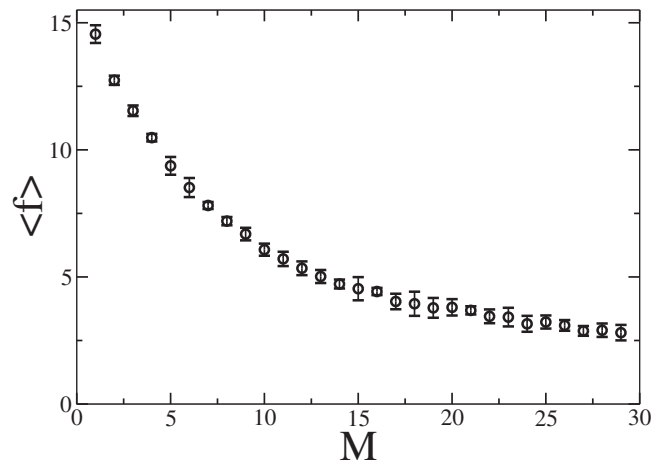


FIG. 14. Dependence of mean finger number $\langle f \rangle$ of the final dried-in structures on particle mobility M . Every data point corresponds to the mean value of seven simulations; error bars indicate the corresponding standard deviation. The remaining parameters are as in Fig. 13.

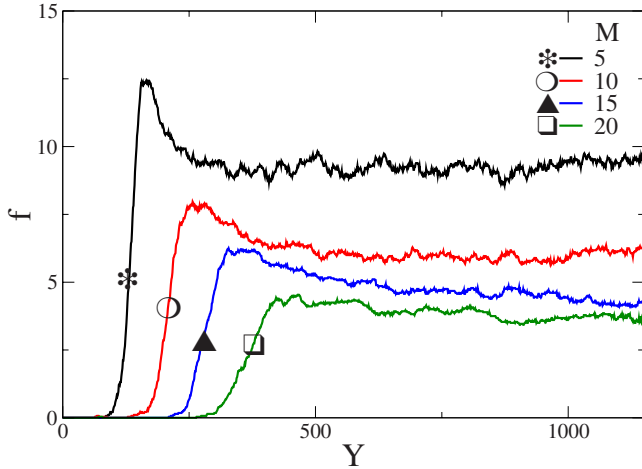


FIG. 15. (Color online) Dependence of finger number on streamwise coordinate (i.e., y direction) for various values of mobility as given in the legend. As the structures are fixed when they stay behind the front, increasing y also indicates increasing time. Each curve corresponds to the average of 28 runs. The remaining parameters are as in Fig. 13.

particle concentrations. This resembles the situation in the experiments and was also used in most computations in Refs. [26,29].

In the following we will analyze the influence of ϵ_{nn} and ϵ_{nl} on the fingering instability. In particular, we are interested in a possible coupling of the front instability and the demixing of particles and liquid. In our scaling ($\epsilon_{\eta}=1$), demixing will occur for large ϵ_{nn} (at fixed ϵ_{nl}) or small ϵ_{nl} (at fixed ϵ_{nn}), i.e., for large ratios $\epsilon_{nn}/\epsilon_{nl}$.

Figure 17 presents results for the average number of fingers when ϵ_{nn} is changed, in the range between 1.4 and 2.5. Inspecting the figure, one can distinguish four regions.

(i) At small $\epsilon_{nn} < 1.95$ the particular strength of the interaction has nearly no influence; only a slight decrease of the finger number with increasing ϵ_{nn} is discernible. We call this the “transport regime” as only the transport properties play a role.

(ii) In an intermediate region $1.95 < \epsilon_{nn} < 2.15$ the finger number increases steeply by about a factor of 3. Fingers emerge at the receding front and there is no demixing at all going on in the liquid bulk behind the front. What we see is still a pure front instability that is, however, strongly influenced by the ratio of interaction parameters. We interpret this as a front-induced demixing that leads to fingering. In other words, the front itself acts as a “nucleation site” for demixing. We call this a “demixing-induced front instability.” Note, however, that fingering still leads to a strongly anisotropic fingering pattern. Although the fingers break at some places they do not in general break up into small nanoparticle islands.

(iii) With further increase of ϵ_{nn} above 2.15, the finger number decreases again till about $\langle f \rangle = 15$ at about $\epsilon_{nn} = 2.25$. This is mainly a geometric effect resulting from our one-dimensional finger-counting routine. It reflects the fact that the fingers break up increasingly and the dried-in nanoparticle pattern starts to look more and more isotropic. Demixing of particles and liquid occurs already in the bulk liquid behind the front.

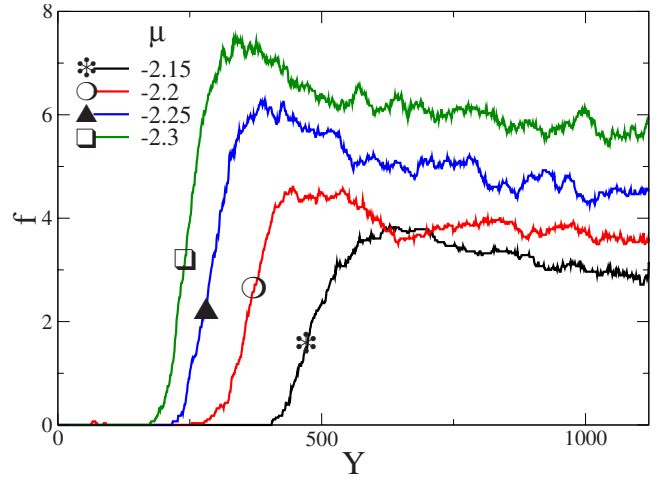


FIG. 16. (Color online) Dependence of finger number on streamwise coordinate (i.e., y direction) for various values of the chemical potential as given in the legend. Each curve corresponds to the average of 28 runs. The remaining parameters are as in Fig. 9.

(iv) Beyond $\epsilon_{nn}=2.25$ fluid and particles demix already in the bulk in a homogeneous manner, the remaining dried-in structure of nanoparticle islands is isotropic, and the emerging demixing length scale decreases with increasing ϵ_{nn} . The finger number is one way to count the islands. Note, however, that it is not an adequate measure to study those isotropic structures (which are not of central interest here). The front resembles a liquid front receding inside a porous medium (formed by the nanoparticle islands).

Our interpretation of the ongoing physical processes is confirmed by Fig. 18 showing the dependence of the average

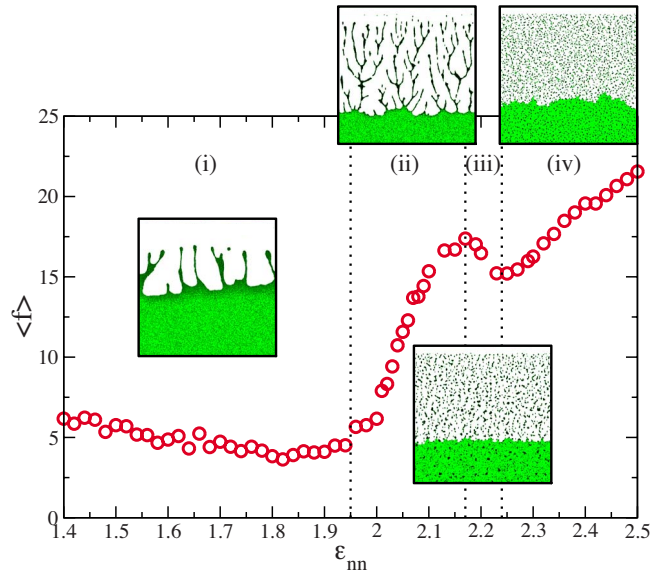


FIG. 17. (Color online) Dependence of the mean finger number on the particle-particle interaction strength ϵ_{nn} . The regions marked (i)–(iv) are discussed in the main text. The remaining parameters are domain size 1200×1200 , $kT=0.2$, $M=20$, $\mu=-2.2$, $\phi=0.1$, $\epsilon_{nl}=1.5$. The insets give typical snapshots obtained in the four different regions. Particles are black, liquid is gray (green online), and empty substrate is white.

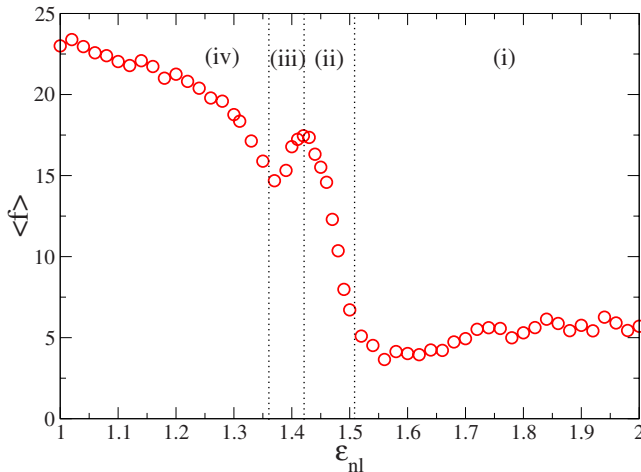


FIG. 18. (Color online) Dependence of the mean finger number on the particle-liquid interaction strength ϵ_{nl} . The regions marked (i)–(iv) are discussed in the main text. The remaining parameters are as in Fig. 17, and $\epsilon_{nn}=2.0$.

number of fingers on the liquid-particle interaction strength ϵ_{nl} in the range between 1.0 and 2.0 for fixed $\epsilon_{nn}=2.0$. A similar sequence of regions (i)–(iv) is found; this time, however, with decreasing interaction parameter. This agrees well with the considerations at the start of this section.

VI. CONCLUSIONS

The present work has focused on pattern formation observed in various experimental settings involving dewetting and drying nanofluids on solid substrates. In addition to polygonal networks and spinodal-like structures, branched structures have been reported in the experiments. We have employed a kinetic Monte Carlo model to study pattern formation driven by the interplay of evaporating solvent and diffusing nanoparticles. A justification of the usage of a model that includes dewetting only by evaporation but not by convective motion of the solvent has been given based on experimental observations and scaling considerations derived from a mesoscopic continuum model.

The model has first been used to analyze the influence of the nanoparticles on the basic dewetting behavior, i.e., on spinodal dewetting and also on dewetting by nucleation and growth of holes. It has been found that the “classical” hypothesis that the solute mainly decorates and conserves the volatile dewetting structures of the solvent has to be amended in some important regions of parameter space. While it is true that the nanoparticles help to image the basic dewetting patterns (such as the labyrinthine structure resulting from spinodal evaporative dewetting or the random polygonal network resulting from nucleation and growth), they *shift* the bimodal and spinodal line in the chemical potential by a small amount that can be estimated using a mean-field argument. In consequence, they influence the nucleation rate. Although in the present work we have not focused on this aspect, it should be further scrutinized in the future. More importantly, the nanoparticles strongly destabilize straight or circular dewetting fronts in the nucleation regime. The main

body of the paper has entirely focused on a numerical study of the underlying transverse front instability.

We have analyzed the dependence of the characteristics of the branching patterns on the driving effective chemical potential, the mobility or diffusivity of the nanoparticles, and their concentration. As a result we have found that the mean number of fingers is almost independent of the particle concentration. At a higher concentration one finds a very similar number of slightly thicker fingers. The most influential parameters are the particle diffusivity and the chemical potential. A decreasing chemical potential (mobility) leads to denser [less dense] finger patterns that develop earlier [later]. Note that a decreasing chemical potential corresponds to an increasing driving force, i.e., to a larger mean velocity of the dewetting front. As a result, we have drawn the conclusion that the crucial factor determining the instability characteristics is the ratio of the time scales of the different transport processes. In particular, a small ratio of the velocity of the dewetting front and the mean diffusion velocity of the particles renders the front more unstable. If the particle diffusivity is too low the particles are collected at the front. In consequence, the front is slowed down, and an unstable stratification of concentration evolves: Any fluctuation in concentration along the front will trigger a transverse instability that results in an evolving fingering pattern. This process can be seen as a self-optimization of the front motion. The average front velocity is kept constant by expelling particles into fingers that stay behind. In this way the mean velocity is maintained at a nearly constant value. A similar effect was previously described for dewetting non-volatile polymer films [21]. There, the dewetting front expels liquid from the growing rim, which collects the dewetted polymer, and the liquid is left behind in the form of deposited droplets. The present system, however, allows one to study the branching of the finger structure also.

In addition to the dependencies on particle density, mobility, and driving force, we have also investigated the influence of the energetics of the system, i.e., the dependence of the fingering on the interaction strengths. We were especially interested in a possible coupling between front motion and instability on the one hand and a liquid-particle demixing on the other hand. On physical grounds we have distinguished three different regimes. At small particle-particle interaction strength or large particle-liquid interaction strength the fingering is nearly independent of the interaction constants. That is, it is a purely dynamic instability. We have called this the transport regime. At large particle-particle interaction strength or small particle-liquid interaction strength, demixing of liquid and particles occurs already in the bulk liquid. The retraction of the liquid front then resembles the dewetting of a two-dimensional porous medium. At intermediate interaction strengths, the finger density strongly depends on the energetics of the system. We have found that particles and liquid demix at the moving front, rendering it transversely unstable. The resulting length scale is determined by the dynamics and the energetics of the system. We have called this a demixing-induced front instability.

In the light of the numerical findings presented here, the experimental results described above may be understood in terms of changes in nanoparticle mobility resulting from dif-

ferences in the length of the carbon chains of the thiol ligands and the interpenetration of the ligands of different particles. Particles with short thiol chains diffuse faster and interpenetrate less. Therefore nearly no fingering is observed for C_5 and C_8 . Longer chains lead to slower diffusion, implying better developed fingers for C_{10} and C_{12} . It is likely that the decrease in fingering for C_{14} -passivated nanoparticles results on the one hand from end gauche defects in C_{14} chains that tend to produce less pronounced interdigitation than for C_{12} thiols [31]. On the other hand, longer chain length will also lead to greater core-core separation. This might drive ϵ_{nn} down and shift the system from a demixing-induced front instability towards the transport regime where the finger number is lower. The present experiments, however, do not allow a direct comparison of finger numbers with the simulations as the radial geometry of the normal nucleated holes does not facilitate a quantitative analysis. Future experiments that study fingering using imposed straight dewetting fronts would be of high interest.

We based the quantitative analysis of the fingering on the assumption of stationarity of the fingering process, i.e., on the assumption that the main properties of the pattern do not depend on the streamwise position. A detailed test of the assumption has shown that it is valid as the fingering pattern is stationary after an initial exponential growth in finger number that peaks at a maximal value before settling on a slightly lower level via finger coarsening. Following the transient phase, the finger density fluctuates around a stationary state. This observation not only validates the quantification used but also confirms the hypothesis of auto-optimization of the front velocity: the front collects particles at a constant rate and leaves them behind in deposited fingers at the same rate. However, not only is the overall rate stationary but so the spatial distribution of fingers are as well, and its dynamics including the creation of new fingers (finger tips) and the annihilation of fingers by merging (branching points).

We have checked that the results obtained are generic in the sense that small changes in the model setup do not change the behavior qualitatively. In particular, we used an independently written code for 1×1 nanoparticles to ensure that the nanoparticle size is not a crucial element. The present work assumed 3×3 nanoparticles to allow for simple comparison with already published results [26,27,29]. To reach the same density of fingers for 1×1 nanoparticles, the mobility has to be smaller than in the 3×3 case.

A crucial rule used in the algorithm is the contrast in the mobility of the nanoparticles, i.e., the assumption that they do not diffuse onto the dry substrate. If one lifts this rule and tries to bound the nanoparticles more strongly into the liquid by increasing the particle-liquid interaction strength, i.e., one strongly increases the energetic bias of the particles toward the retracting liquid, no front instability is found. This explains why Ising-type models for grain growth that include mobile diffusing impurities, to our knowledge, have never reported instabilities of domain boundaries caused by the diffusing impurities [70–72]. In all these models the impurities diffuse equally well in the two phases. They might, however, be energetically biased toward one of the phases or toward the phase boundary. Our present results on evaporating nanoparticle solutions suggest that unstable domain

boundaries might also be found in the ordering dynamics of a ferromagnetic system with diffusing impurities under the influence of an external field if the mobility of the impurities strongly depends on the phase.

Finally, we discuss the limitations of the Monte Carlo method we have used. These arise from the assumptions that the dominant processes can be captured in a two-dimensional setting, neglecting the film thickness of the evaporating film, and that the only relevant dynamics corresponds to particle diffusion and solvent evaporation. It was argued above, based on the general structure of a thin film model, that for film thicknesses below 10 nm, the convective motion of the solution can be neglected as compared to the effect of evaporation. We have also laid out in what way recent experiments support this approximation. However, the experiments clearly show effects that cannot be described by employing the present model. On the one hand, there are effects associated with the macroscopic dewetting front which recedes before the ultrathin postcursor film evaporatively dewets (and thus produces the different types of structure described here and elsewhere using variants of the two-dimensional kinetic Monte Carlo model [26,27,29,31,60]). The macroscopic front can as well be unstable. That instability, however, obviously involves the convective motion of the solution and can not be described with the present model. In the last three panels of Fig. 1 one notices the superposition of large and small-scale network structures. The present model is able to describe the small-scale network. The evolution of the large-scale (mesoscopic) network, however, occurs at larger film thicknesses and involves convective motion of the solvent. Different models are necessary to describe those processes. Several mesoscale dynamic models such as, e.g., a dynamic density functional theory for nanoparticle and liquid densities and thin film models are possible candidates and will be investigated in the future.

Note that a good mesoscopic thin film model should explain the existence of the ultrathin postcursor film. Here we have taken its existence for granted based on experimental observation [31], and have justified the model on this basis. The model we have used, however, cannot explain the existence of the postcursor. A possible hypothesis in this respect is that the nanoparticles are strongly attracted to the substrate and form a denser suspension layer of a thickness that corresponds to the nanoparticle diameter. The mesoscopic dewetting process would then actually correspond to a dewetting of the low-concentration suspension from the high concentration layer. This could be called autophobic behavior. The corresponding disjoining pressure would stabilize the layer with respect to homogeneous evaporation, similar to effects modeled for simple liquids in Ref. [56].

The shortcomings described up to here are related to the exclusion of mesoscopic hydrodynamics from the model. On the other hand, it is obvious that its two-dimensional character restricts the model to a constant interaction of solvent and substrate that is absorbed into the effective chemical potential. Therefore it cannot account for the change of relative

influence of various short- and long-range contributions to this interaction which was shown to be important for films below 10 nm thickness (e.g., [39]). A pseudo-3D kinetic Monte Carlo model has recently been developed that allows the energetic aspect of a thickness-dependent disjoining pressure to be incorporated into an effective chemical potential that depends on the mean concentration of liquid. Such a model is able to model dual-scale structures like large holes

that grow in an unstable manner and are embedded in a pattern of small holes [60].

ACKNOWLEDGMENTS

We acknowledge support by the European Union via the FP6 Marie Curie scheme [Grant No. MRTN-CT-2004005728 (PATTERNS)].

-
- [1] P. Ball, *The Self-Made Tapestry* (Oxford University Press, Oxford, 1999).
- [2] P. G. Saffman and G. Taylor, Proc. R. Soc. London, Ser. A **245**, 312 (1958).
- [3] T. Vicsek, *Fractal Growth Phenomena*, 1st ed. (World Scientific, Singapore, 1989).
- [4] M. Cachile and A. M. Cazabat, Langmuir **15**, 1515 (1999).
- [5] M. Cachile, G. Albiu, A. Calvo, and A. M. Cazabat, Physica A **329**, 7 (2003).
- [6] M. R. E. Warner, R. V. Craster, and O. K. Matar, J. Fluid Mech. **510**, 169 (2004).
- [7] H. E. Huppert, Nature (London) **300**, 427 (1982).
- [8] M. A. Spaid and G. M. Homsy, Phys. Fluids **8**, 460 (1996).
- [9] M. H. Eres, L. W. Schwartz, and R. V. Roy, Phys. Fluids **12**, 1278 (2000).
- [10] S. Kalliadasis, J. Fluid Mech. **413**, 355 (2000).
- [11] U. Thiele and E. Knobloch, Phys. Fluids **15**, 892 (2003).
- [12] A. M. Cazabat, F. Heslot, S. M. Troian, and P. Carles, Nature (London) **346**, 824 (1990).
- [13] J. B. Brzoska, F. Brochard-Wyart, and F. Rondelez, Europhys. Lett. **19**, 97 (1992).
- [14] A. L. Bertozzi, A. Münch, X. Fanton, and A. M. Cazabat, Phys. Rev. Lett. **81**, 5169 (1998).
- [15] F. Melo, J. F. Joanny, and S. Fauve, Phys. Rev. Lett. **63**, 1958 (1989).
- [16] G. Reiter, Langmuir **9**, 1344 (1993).
- [17] A. Sharma and G. Reiter, J. Colloid Interface Sci. **178**, 383 (1996).
- [18] S. Herminghaus, A. Fery, S. Schlagowski, K. Jacobs, R. Seemann, H. Gau, W. Mönch, and T. Pompe, J. Phys.: Condens. Matter **12**, A57 (2000).
- [19] M. Elbaum and S. G. Lipson, Phys. Rev. Lett. **72**, 3562 (1994).
- [20] H. I. Kim, C. M. Mate, K. A. Hannibal, and S. S. Perry, Phys. Rev. Lett. **82**, 3496 (1999).
- [21] G. Reiter and A. Sharma, Phys. Rev. Lett. **87**, 166103 (2001).
- [22] U. Thiele, Eur. Phys. J. E **12**, 409 (2003).
- [23] W. M. Gelbart, R. P. Sear, J. R. Heath, and S. Chaney, Faraday Discuss. **112**, 299 (1999).
- [24] G. L. Ge and L. Brus, J. Phys. Chem. B **104**, 9573 (2000).
- [25] P. Moriarty, M. D. R. Taylor, and M. Brust, Phys. Rev. Lett. **89**, 248303 (2002).
- [26] C. P. Martin, M. O. Blunt, and P. Moriarty, Nano Lett. **4**, 2389 (2004).
- [27] C. P. Martin, M. O. Blunt, E. Pauliac-Vaujour, A. Stannard, P. Moriarty, I. Vancea, and U. Thiele, Phys. Rev. Lett. **99**, 116103 (2007).
- [28] G. Yosef and E. Rabani, J. Phys. Chem. B **110**, 20965 (2006).
- [29] E. Rabani, D. R. Reichman, P. L. Geissler, and L. E. Brus, Nature (London) **426**, 271 (2003).
- [30] C. G. Sztrum, O. Hod, and E. Rabani, J. Phys. Chem. B **109**, 6741 (2005).
- [31] E. Pauliac-Vaujour, A. Stannard, C. P. Martin, M. O. Blunt, I. Notinger, P. J. Moriarty, I. Vancea, and U. Thiele, Phys. Rev. Lett. **100**, 176102 (2008).
- [32] R. D. Deegan, O. Bakajin, T. F. Dupont, G. Huber, S. R. Nagel, and T. A. Witten, Nature (London) **389**, 827 (1997).
- [33] R. D. Deegan, Phys. Rev. E **61**, 475 (2000).
- [34] R. D. Deegan, O. Bakajin, T. F. Dupont, G. Huber, S. R. Nagel, and T. A. Witten, Phys. Rev. E **62**, 756 (2000).
- [35] L. V. Govor, G. Reiter, J. Parisi, and G. H. Bauer, Phys. Rev. E **69**, 061609 (2004).
- [36] J. Huang, F. Kim, A. R. Tao, S. Connor, and P. Yang, Nature Mater. **4**, 896 (2005).
- [37] M. Mertig, U. Thiele, J. Bradt, G. Leibiger, W. Pompe, and H. Wendrock, Surf. Interface Anal. **25**, 514 (1997).
- [38] M. Mertig, U. Thiele, J. Bradt, D. Klemm, and W. Pompe, Appl. Phys. A: Mater. Sci. Process. **66**, S565 (1998).
- [39] U. Thiele, M. Mertig, and W. Pompe, Phys. Rev. Lett. **80**, 2869 (1998).
- [40] O. Karthaus, L. Grasjö, N. Maruyama, and M. Shimomura, Chaos **9**, 308 (1999).
- [41] X. Gu, D. Raghavan, J. F. Douglas, and A. Karim, J. Polym. Sci., Part B: Polym. Phys. **40**, 2825 (2002).
- [42] L. V. Govor, J. Parisi, G. H. Bauer, and G. Reiter, Phys. Rev. E **71**, 051603 (2005).
- [43] P. Müller-Buschbaum, E. Bauer, S. Pfister, S. V. Roth, M. Burghammer, C. Riekkel, C. David, and U. Thiele, Europhys. Lett. **73**, 35 (2006).
- [44] M. D. Haw, M. Gillie, and W. C. K. Poon, Langmuir **18**, 1626 (2002).
- [45] E. Bormashenko, R. Pogreb, O. Stanevsky, Y. Bormashenko, T. Stein, V. Z. Gaisin, R. Cohen, and O. V. Gendelman, Macromol. Mater. Eng. **290**, 114 (2005).
- [46] E. Bormashenko, R. Pogreb, O. Stanevsky, Y. Bormashenko, T. Stein, and O. Gengelman, Langmuir **21**, 9604 (2005).
- [47] P.-G. de Gennes, Rev. Mod. Phys. **57**, 827 (1985).
- [48] G. Reiter, Phys. Rev. Lett. **68**, 75 (1992).
- [49] R. Seemann, S. Herminghaus, C. Neto, S. Schlagowski, D. Podzimek, R. Konrad, H. Mantz, and K. Jacobs, J. Phys.: Condens. Matter **17**, S267 (2005).
- [50] U. Thiele, Ph.D. thesis, Technische Universität Dresden, 1998.
- [51] E. Pauliac-Vaujour and P. Moriarty, J. Phys. Chem. C **111**, 16255 (2007).

- [52] C. Gigault, K. Dalnoki-Veress, and J. R. Dutcher, *J. Colloid Interface Sci.* **243**, 143 (2001).
- [53] Nanolane (see <http://www.nano-lane.com>).
- [54] A. Oron, S. H. Davis, and S. G. Bankoff, *Rev. Mod. Phys.* **69**, 931 (1997).
- [55] *Thin Films of Soft Matter*, edited by S. Kalliadasis and U. Thiele (Springer, Vienna, 2007).
- [56] A. V. Lyushnin, A. A. Golovin, and L. M. Pismen, *Phys. Rev. E* **65**, 021602 (2002).
- [57] L. M. Pismen, *Phys. Rev. E* **70**, 021601 (2004).
- [58] J. N. Israelachvili, *Intermolecular and Surface Forces* (Academic Press, London, 1992).
- [59] V. S. Mitlin, *J. Colloid Interface Sci.* **156**, 491 (1993).
- [60] A. Stannard, C. P. Martin, E. Pauliac-Vaujour, P. Moriarty, and U. Thiele, *J. Phys. Chem. C* **112**, 15195 (2008).
- [61] A. Chatterjee and D. G. Vlachos, *J. Comput.-Aided Mater. Des.* **14**, 253 (2007).
- [62] K. A. Fichthorn and W. H. Weinberg, *J. Chem. Phys.* **95**, 1090 (1991).
- [63] H. C. Kang and W. H. Weinberg, *J. Chem. Phys.* **90**, 2824 (1989).
- [64] M. I. Larsson, *Phys. Rev. B* **64**, 115428 (2001).
- [65] L. A. Ray and R. C. Baetzold, *J. Chem. Phys.* **93**, 2871 (1990).
- [66] L. Onsager, *Phys. Rev.* **65**, 117 (1944).
- [67] J. S. Langer, in *Solids far from Equilibrium*, edited by C. Godreche (Cambridge University Press, Cambridge, U.K., 1992), pp. 297–363.
- [68] U. Thiele, M. G. Velarde, and K. Neuffer, *Phys. Rev. Lett.* **87**, 016104 (2001).
- [69] U. Thiele, M. G. Velarde, K. Neuffer, and Y. Pomeau, *Phys. Rev. E* **64**, 031602 (2001).
- [70] D. J. Srolovitz and G. N. Hassold, *Phys. Rev. B* **35**, 6902 (1987).
- [71] E. Vives and A. Planes, *Phys. Rev. Lett.* **68**, 812 (1992).
- [72] H. Gilhoj, C. Jeppesen, and O. G. Mouritsen, *Phys. Rev. E* **52**, 1465 (1995).